Journal of MATERIALS RESEARCH

Article
DOI: 10.1557/jmr.2019.267

# Graphene/chitosan-functionalized iron oxide nanoparticles for biomedical applications

Suresh Bandi[1,b], Vikram Hastak[1,b], Chokkakula L.P. Pavithra[2], Sanjay Kashyap[3], Dhananjay Kumar Singh[4], Suaib Luqman[5], Dilip R. Peshwe[1], Ajeet K. Srivastav[1,a]

[1]*Department of Metallurgical and Materials Engineering, VNIT Nagpur, Maharashtra 440010, India*
[2]*Department of Materials Science and Metallurgical Engineering, IIT Hyderabad, Telangana 502285, India*
[3]*School of Physics and Materials Science, Thapar Institute of Engineering and Technology, Patiala, Punjab 147004, India*
[4]*Department of Molecular Bioprospection, CSIR-Central Institute of Medicinal and Aromatic Plants, Lucknow, Uttar Pradesh 226002, India; and Department of Human Molecular Genetics and Biochemistry, Sackler School of Medicine, Tel Aviv University, Tel Aviv 699780, Israel*
[5]*Department of Molecular Bioprospection, CSIR-Central Institute of Medicinal and Aromatic Plants, Lucknow, Uttar Pradesh 226002, India*
[a)]Address all correspondence to this author. e-mail: srivastav.ajeet.kumar@gmail.com, ajeet.srivastav@mme.vnit.ac.in
[b)]These authors contributed equally to this work.

Received: 18 March 2019; accepted: 20 August 2019

**Superparamagnetic iron oxide nanoparticles are well known for biomedical applications. The particle size, morphology, surface area, and functionalization are the key parameters that affect their bioactivity properties. Inline to this, the superparamagnetic $Fe_3O_4$ nanoparticles were prepared via chemical coprecipitation method with an average particle size of 6 ± 3 nm. The particles were surface-functionalized with chitosan and in-house prepared reduced graphene oxide (rGO) to obtain chitosan-coated $Fe_3O_4$ nanoparticles (C-$Fe_3O_4$) and rGO-$Fe_3O_4$ nanocomposites (G-$Fe_3O_4$), respectively. Upon functionalization, the physicochemical properties of the materials were characterized thoroughly using X-ray diffraction, transmission electron microscopy, vibrating sample magnetometer, Raman Spectroscopy, and thermal gravimetric analysis. Furthermore, they have subjected to cytotoxicity assay, agar two-fold broth dilution test, and disc diffusion assay experiments for the determination of cytotoxicity and antibacterial activities. The effect of surface functionalization on their bioactivity was investigated thoroughly. The surface functionalization with chitosan and rGO has enhanced the bioactivity of the $Fe_3O_4$ nanoparticles.**

## Introduction

Iron oxide nanoparticles (IONPs), owing to their superparamagnetic behavior, have shown great potential toward biomedical applications for decades by competing with a variety of biocompatible nanoparticles viz., magnetic nanoparticles, gold nanoparticles, core–shell quantum dots, carbon nanoparticles, rare earth nanoparticles, polymers, and liposomes [1]. The promising features like tunability in size [2], shape [3], and surface [4] make the IONPs versatile and candidate material for various applications like high-density magnetic storage [5], magnetic catalysis [6], water splitting [7, 8], and biomedicine [9, 10]. Besides, the IONPs synthesized with enhanced biocompatibility are being used in various biomedical applications including *in vivo* magnetic resonance imaging (MRI) [11, 12, 13], magnetic particle imaging (MPI) [14, 15, 16], *in vitro* bioseparation [17, 18], targeted *in vivo* drug delivery [19], and hyperthermia [20].

In targeted drug delivery, IONPs are usually tagged to specific biological molecules (drugs) to target malignant tissues inside the human body [9, 19, 21]. An external magnetic field will control the targeted IONPs. In general, the agglomeration is the most common issue possessed by nanoparticles due to their higher surface energies. However, the efficient biocompatibility could be achieved by preventing agglomeration by surface functionalization of IONPs. Chitosan (poly-β-(1-4)-2-amino-2-deoxy-D-glucose) is a widely accepted surface functionalizing agent among existing polymeric and nonpolymeric agents, owing to its low cost, biocompatibility, nontoxicity, chemical stability, thermal stability, and cation characteristics [22]. Coating of IONPs with chitosan results into IONPs of a magnetic core with biodegradable chitosan shell. The magnetic behavior of IONPs helps in targeting drugs to a specific site through an external magnetic field. Whereas biodegrading behavior of chitosan shell leads to the release and transport of

https://doi.org/10.1557/jmr.2019.267 Published online by Cambridge University Press



© Materials Research Society 2019

drugs which are already loaded to these chitosan-functionalized IONPs [21]. These targeted IONPs can be even separated from biological drugs through magnetic separation and reused.

Once efficient targeting is achieved, IONPs adds to the utility of drugs in the treatment of harmful cells, thus reducing the overall dosage. Usually, cancerous cells and bacteria have a net negative charge on their surface. Their growth rate can be mitigated or inhibited upon interaction with drugs (containing a net surface positive charge) by being antiproliferative or cytotoxic based on their interaction and dosage level of drugs. A variety of cell proliferative studies [23] are in practice to investigate the effect of IONPs on the minimization of dosage required, and the health issues can rise during drug targeting. On the other hand, various screening methods also have been reported so far for quantifying antibacterial activity [24] of as-synthesized agents.

Graphene also has gained significant attention in this scenario. The surface contact–based bioactivity of graphene-based materials through the possible generation of reactive oxygen species (ROS) made them candidate materials for cytotoxicity-based studies [25, 26]. The significant results of graphene and graphene combined with IONPs in the current context were reported elsewhere [27, 28, 29, 30, 31, 32]. Jedrzejczak-Silicka et al. [31] investigated the effect of graphene with $Fe_3O_4$ on relative viability and DNA integrity. They summarized that this material showed excellent biocompatibility. Furthermore, they reported the potentiality of the material for hyperthermia treatment. Gade et al. [32] reported the dose-dependent cytotoxic effects of graphene oxide–$Fe_2O_3$ nanoparticles on Wharton's jelly-derived mesenchymal stem cells (WJ-MSCs). The GO–$Fe_2O_3$ showed less impact on cellular morphology, viability, clonigenic property, and growth kinetics of caprine WJ-MSCs. Negative impact on these parameters was increased with the dose of GO–$Fe_2O_3$.

In the current work, $Fe_3O_4$ nanoparticles were prepared via facile chemical coprecipitation method. The nanoparticles were functionalized with chitosan, and in-home prepared rGO. The advanced characterization tools and techniques were used to understand how the inherent behavior or properties of the materials are related to cytotoxicity and antibacterial activities. The materials were analyzed rigorously for phase and crystal structure investigations, particle size analysis, magnetic behavior, and chemical stability. Their cytotoxicity and antibacterial activities were investigated individually against various cell lines and bacteria. Finally, the effect of functionalization with chitosan and graphene on these cytotoxicity and antibacterial activities were correlated.

## Results and discussion

### Characterization

#### XRD

Figure 1(a) shows the XRD spectra of $Fe_3O_4$ nanoparticles. The XRD profile of $Fe_3O_4$ nanoparticles was well matched with the reference pattern (ICSD reference code 98-015-8505) [33]. The quantification of structural parameters like crystallite size was carried through adopting line profile analysis (LPA). The structural analysis was done by fitting XRD spectra with pseudo-Voigt function. In the abovementioned LPA, integral breadth will be considered as a measure of peak width and universal shape factor considers for peak shape variation. The instrumental broadening was subtracted with a silicon standard sample, which was fitted by the same pseudo-Voigt profile fitting function. The details of complete profile fitting parameters have been discussed elsewhere [34, 35, 36]. The crystallite size (coherently diffracted domains) and its distribution were evaluated by double-Voigt analysis as reported by Balzar and Ledbetter [37]. The Breadth program by Balzar was used here for the crystallite size distribution by taking

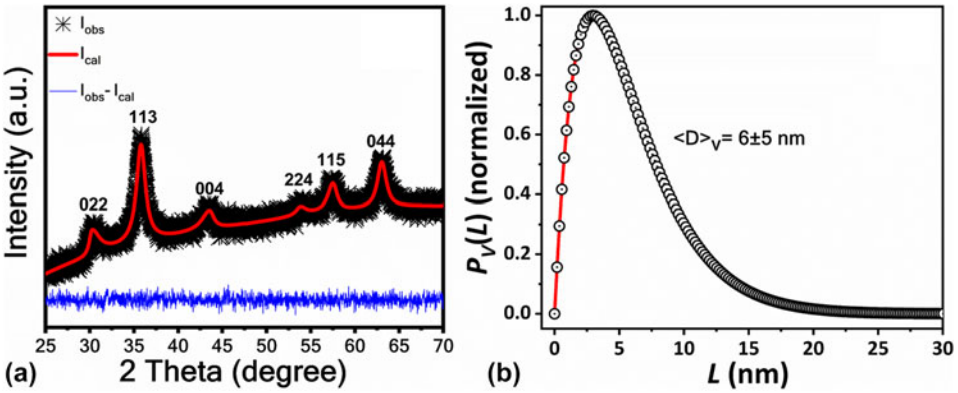



**Figure 1:** (a) XRD spectra of $Fe_3O_4$ nanoparticles with LPA and (b) crystallite size distribution using double-Voigt analysis by Breadth program. $I_{obs}$ corresponds to the intensity obtained from the sample. $I_{calc}$ is the intensity of the profile after pseudo-Voigt function fitting. $I_{obs} - I_{calc}$ is the difference plot of observed and calculated profiles.

https://doi.org/10.1557/jmr.2019.267 Published online by Cambridge University Press



© Materials Research Society 2019

full-width at half-maximum (FWHM) and mixing parameter (η) of LPA fitted XRD profiles as input parameters [38, 39]. The crystallite size was evaluated to be 6 ± 5 nm, and the distribution was as shown in Fig. 1(b).

## TEM

The elemental distribution of Fe and O in $Fe_3O_4$ system was examined with the help of high-angle annular dark-field scanning transmission electron microscopy (HAADF-STEM) [coupled with energy dispersive spectroscopy (EDS)]. Figure 2 shows the HAADF-STEM images of the Fe [Fig. 2(b)], O [Fig. 2(c)], and the overlay of Fe and O [Fig. 2(d)] for the selected area [Fig. 2(a)] in the sample. The elemental mapping revealed that the distribution of Fe and O in $Fe_3O_4$ are consistent.

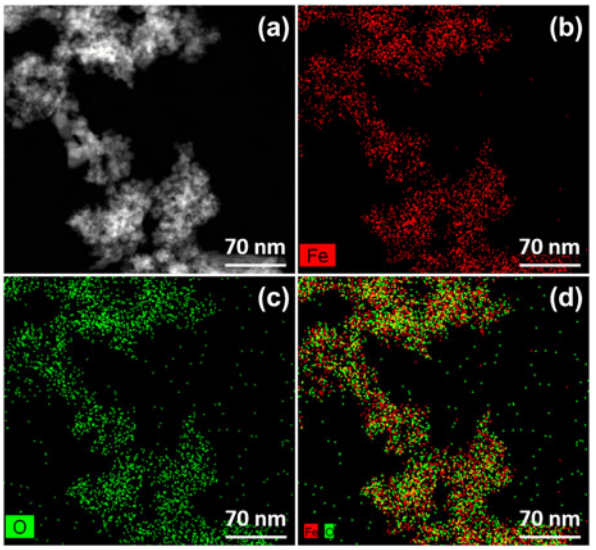



**Figure 2:** STEM-HAADF elemental mapping of $Fe_3O_4$ nanoparticles (a) HAADF-STEM image of the selected area for elemental mapping, (b) the mapping indicating for Fe, (c) the mapping of oxygen, and (d) the overlay of both Fe and O.

Whereas Fig. 3 shows the dark-feld image of $Fe_3O_4$ nanoparticles (a), corresponding selected area electron diffraction (SAED) ring pattern (b), and the histogram for particles size distribution. The bright spots in the dark-field image correspond to the most intense ring (113) from the electron diffraction pattern (indexed with red mark). The size of the particles was varying between 2 and 16 nm. Thus, the histogram was made with the collected data of each particle's size to measure the average particle size. The average size of the particles from the size histogram was found to be 6 ± 3 nm, which is in line with the crystallite size measured through Balzar's breadth program (6 ± 5 nm). As the crystallite size is similar to the particle size, the particles formed in this process could be the single-crystal nanoparticles of $Fe_3O_4$. The high-resolution transmission electron microscopy (HRTEM) images, corresponding to the selected area of diffraction patterns (of red square in HRTEM images), and their inverse fast Fourier transform (IFFT) HRTEM images are illustrated in Figs. 4(a) and 4(b), respectively. The *d*-spacing measurements for the corresponding planes in the IFFT patterns were in good agreement with the reference pattern.

## VSM

The superparamagnetism of $Fe_3O_4$ and G-$Fe_3O_4$ was examined through *M*–*H* hysteresis curve obtained through vibrating

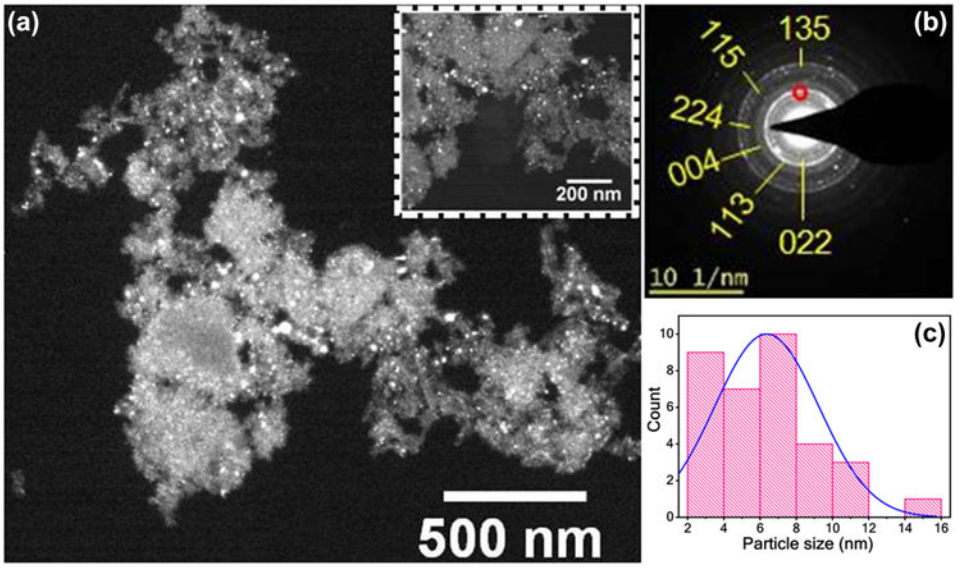



**Figure 3:** (a) Dark-field TEM image of $Fe_3O_4$ nanoparticles, (b) SAED pattern indexed with planes corresponding to $Fe_3O_4$ inverse spinel structure, and (c) size distribution of $Fe_3O_4$ nanoparticles showing average particle size 6 ± 3 nm.

https://doi.org/10.1557/jmr.2019.267 Published online by Cambridge University Press



© Materials Research Society 2019

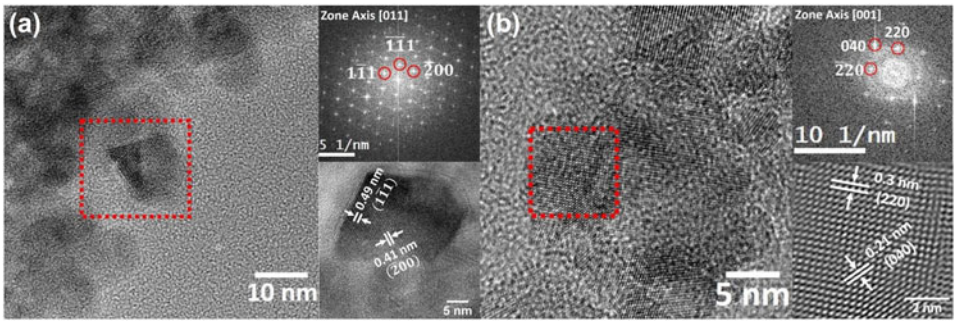



**Figure 4:** (a) and (b) High-resolution TEM micrographs of $Fe_3O_4$ nanoparticles with indexed FFT patterns of the selected area (red square) and corresponding noise-corrected lattice images.

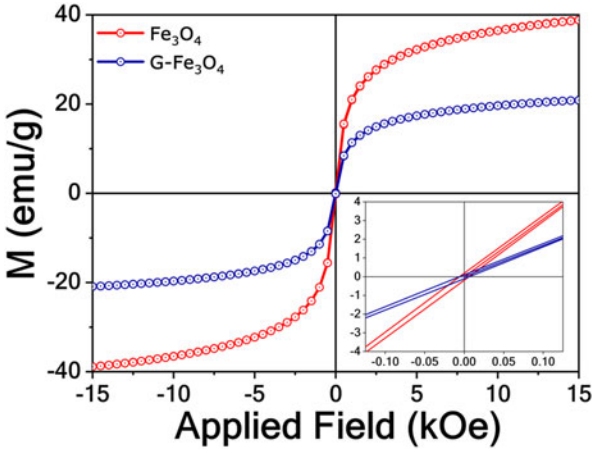



**Figure 5:** The *M–H* hysteresis curve obtained by VSM for $Fe_3O_4$ and G-$Fe_3O_4$. The inset shows the magnified portion of the curve near the origin. The magnetization curve with almost closed hysteresis loop can be attributed to the superparamagnetic behavior of $Fe_3O_4$ and G-$Fe_3O_4$.

sample magnetometer (VSM) as shown in Fig. 5. The magnetization curve with nearly closed hysteresis loop shows the superparamagnetic nature of both materials. The values of saturation magnetization ($M_s$) and coercivity for $Fe_3O_4$ nanoparticles were found to be as 39 emu/g and 6.09 Oe, respectively. Whereas G-$Fe_3O_4$ possessed 20.1 emu/g saturation magnetization and 6.25 Oe coercivity, respectively. The near-zero value of remnant magnetization (retentivity) indicates zero magnetization of the samples on the removal of the external field [40].

The theoretical value of saturation magnetization for bulk $Fe_3O_4$ is said to be 96 emu/g. The decreased saturation magnetization values were obtained for both $Fe_3O_4$ and G-$Fe_3O_4$. The decrease in saturation magnetization could be possible with reduced particle size, surface disorders, cation distributions, and adsorbed moisture over the particle surfaces. These reasons could be affected to the extent of creating a dead magnetic layer over the particle surfaces. Thus, the saturation magnetization comes down [41]. The same could be happened in case of C-$Fe_3O_4$ due to the presence of nonferromagnetic organic layer around the particle and exhibiting individual particle nature due to functionalization [42, 43, 44]. As the $Fe_3O_4$ particles in the current study are in the nanodomain (6 nm), the moisture adsorption could be higher because of their higher surface energies. Consequently, the saturation magnetization might get decreased. The addition of nonmagnetic materials, i.e., rGO further decreased its saturation magnetization in G-$Fe_3O_4$. However, both the materials have retained the superparamagnetic behavior.

## Raman spectroscopy

The Raman spectra of carbon/graphene-based materials can be explained by their characteristic peaks, namely, D-band, G-band, and 2D-band. These bands reveal vibrational phonon scattering characteristics as well as the electronic structure of graphene [45]. The D-band of rGO points out structural defects and is related to $sp^3$ carbon atoms that might result from oxidation of $sp^2$ carbon atoms. The G-band is the characteristics of $sp^2$ carbon atoms ($E_{2g}$ phonons) that form the skeleton of graphene. The 2D peak, often considered as D-peak of second order, does not necessarily represent defects but is an essential characteristic peak which determines the approximate thickness of graphene layer [46, 47].

Figure 6 shows the Raman spectra of rGO, $Fe_3O_4$, and G-$Fe_3O_4$. The $I_D/I_G$ ratio, which gives $sp^3/sp^2$ carbon atoms ratio, quantifies approximately defects due to oxidation in graphene. $I_D/I_G$ for G-$Fe_3O_4$ was found to be 0.964 as compared with 0.9827 for rGO, which signifies more defects in rGO as a result of prominent oxidation in the carbon structure of rGO [48]; the degree of defects thus can be believed to be less in case of G-$Fe_3O_4$ due to effective functionalization [46]. The $I_{2D}/I_G$ ratio which corresponds to 2-dimensional defects thus quantifying the number of graphene layers was less in case of G-$Fe_3O_4$ (0.995) as compared with rGO (0.814), which can be attributed to the introduction of 2D defects by $Fe_3O_4$ nanoparticles in graphene structure [45, 47, 49].The reduced oxidation defects, as well as the number of graphene layers, provide significant advantages for enhancing bioactivity.

https://doi.org/10.1557/jmr.2019.267 Published online by Cambridge University Press



© Materials Research Society 2019

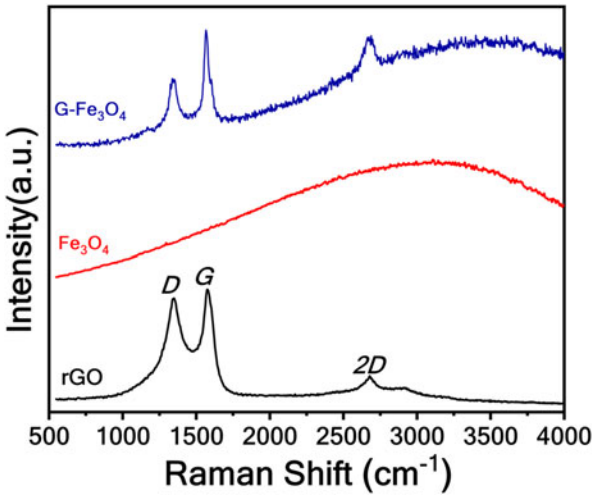



**Figure 6:** Raman spectra of rGO, $Fe_3O_4$, and G-$Fe_3O_4$.

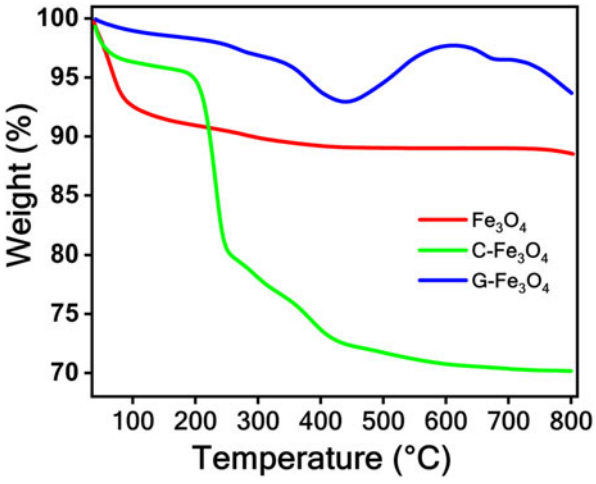



**Figure 7:** TGA profile of $Fe_3O_4$, rGO, and C-$Fe_3O_4$ showing the weight loss with respect to the increasing temperature.

## TGA

The thermal gravimetric analysis (TGA) data of $Fe_3O_4$, C-$Fe_3O_4$, and G-$Fe_3O_4$ are shown in Fig. 7. The mass loss observed at the end of the experiment for $Fe_3O_4$, C-$Fe_3O_4$, and G-$Fe_3O_4$ was 11.49, 29.83, and 6.32%, respectively. The mass loss of C-$Fe_3O_4$ was 2.5 times higher than that of the uncoated $Fe_3O_4$ nanoparticles. The evaporation/degradation of chitosan coated over the $Fe_3O_4$ nanoparticles could be the reason for this excess weight loss. The weight loss occurs before 150 °C attributes to desorption of physisorbed water molecules on the chitosan surface [50]. The sudden drop in the C-$Fe_3O_4$ TGA curve has occurred at 190 °C, and ~15% weight loss was observed in the range of 190–253 °C, which was typical degradation temperature range for chitosan. Hasan et al. [51] reported that the degradation of chitosan would be in two stages, i.e., 150–400 °C and above 400 °C. The first stage of degradation occurs due to depolymerization of chitosan backbone through cleavage of glycosidic linkages. Whereas decomposition of any carbonaceous matter attributes the second stage of degradation. Thus, the weight loss in the range of 150–600 °C could be attributed to the degradation of chitosan. There was a negligible weight loss in the temperature range of 600–800 °C, indicating complete decomposition of chitosan molecules leaving behind $Fe_3O_4$ nanoparticles uncoated. The approximate weight percent of chitosan inferred by comparing the TGA data was found to be approximately 18%. Hence, the TGA data provided evidence for the presence of chitosan coating over $Fe_3O_4$ nanoparticles.

The weight loss of G-$Fe_3O_4$ was very little as compared with the other two materials. The weight loss of 1.77% till 200 °C can be due to the removal of adsorbed moisture. The highest mass loss, i.e., 7.06% in the region of 250–450 °C, can be ascribed to the decomposition of oxygen functional groups and combustion of the carbon [52]. Hence, the presence of rGO in G-$Fe_3O_4$ is evidenced.

## Bioactivity

### *In vitro* cytotoxicity

The results showed that with 2 μg/mL of $Fe_3O_4$, G-$Fe_3O_4$, and C-$Fe_3O_4$, the percent cytotoxicity of the test samples was nearly equivalent, and below 18%. $Fe_3O_4$ and C-$Fe_3O_4$ were not responsive to the PC-3 and K562, respectively. With the increase in concentration to 10 μg/mL, the cytotoxicity of G-$Fe_3O_4$ and C-$Fe_3O_4$ was enhanced as compared with $Fe_3O_4$-alone treated cells. The viability of COLO-205 cell lines reduced to ~22% and ~34% with G-$Fe_3O_4$ and C-$Fe_3O_4$, respectively, and it is reduced to ~30 and ~21% in case of MCF-7 cell lines. When the concentration of the test samples was further increased to 50 μg/mL, bare $Fe_3O_4$ showed ~20–30% cytotoxicity (except MCF-7 cell line for which the value was ~38%), whereas G-$Fe_3O_4$ exhibited 20–40% with almost ~38% for PC-3, A431, COLO-205, and MCF-7. The C-$Fe_3O_4$ showed the highest range of ~40–55% cytotoxicity with a maximum value of ~53% in case of A431 cell line. Also, it has exhibited the highest cytotoxicity in case of all cell lines in comparison to $Fe_3O_4$ and G-$Fe_3O_4$. The performance of G-$Fe_3O_4$ lies between the $Fe_3O_4$ and C-$Fe_3O_4$. It can be concluded that chitosan enhanced the cytotoxicity of $Fe_3O_4$ nanoparticles by approximately two folds, with 50 μg/mL concentration. This can be attributed to the improved surface topography, surface chemistry, and surface energy imparted by chitosan coating over $Fe_3O_4$ nanoparticles, which enhances the cytotoxicity of $Fe_3O_4$ nanoparticles [53].

On the other hand, the increment in the cytotoxicity was not significant when rGO was added to $Fe_3O_4$ nanoparticles. The aggregation of $Fe_3O_4$ over the rGO sheets might have limited the efficient interaction of G-$Fe_3O_4$ against the cell lines [54]. However, the results indicate that increment in the concentration of this sample might increase the cytotoxicity

https://doi.org/10.1557/jmr.2019.267 Published online by Cambridge University Press



© Materials Research Society 2019

appreciably. A critical observation with the addition of rGO to $Fe_3O_4$ nanoparticles is that the increment in cytotoxicity can be attained while ensuring less harm to healthy cells. Figures 8(a), 8(b), and 8(c) shows the cytotoxicity of $Fe_3O_4$, G-$Fe_3O_4$, and C-$Fe_3O_4$, with varying sample concentration against various cell lines.

## Antibacterial activity

The minimum concentration of an antimicrobial drug required to inhibit the visible growth of microorganism is called as minimum inhibitory concentration (MIC) [55]. The antibacterial findings of $Fe_3O_4$, G-$Fe_3O_4$, and C-$Fe_3O_4$ against different Gram-positive and Gram-negative bacteria showed that MIC for bare $Fe_3O_4$ was 1000 μg/mL in most of the tested bacterial strains, except *Staphylococcus aureus*. G-$Fe_3O_4$ also showed the similar results of MIC 1000 μg/mL, except for *Streptococcus pyogenes*. The MIC in case of C-$Fe_3O_4$ was reduced to below (or equal to) 250 μg/mL against all bacteria excluding *Escherichia coli*, for which the MIC was 1000 μg/mL.

The ZOI was also improved upon treatment with G-$Fe_3O_4$ and C-$Fe_3O_4$ as compared with $Fe_3O_4$ alone. However, the response against Gram-negative bacteria *Escherichia coli* was unchanged with chitosan, but with G-$Fe_3O_4$, we observed maximum ZOI in this case. In conclusion, C-$Fe_3O_4$ proved to be the best antibacterial agent than bare $Fe_3O_4$ and G-$Fe_3O_4$ against treated pathogens. Where G-$Fe_3O_4$ stood in-between $Fe_3O_4$ and C-$Fe_3O_4$ in most of the cases, these biological impacts of IONPs may be related with production of excess ROS as well as superoxide radicals ($O^{2-}$), hydroxyl radicals (OH), hydrogen peroxide ($H_2O_2$), and the singlet oxygen ($^1O^2$) which hinders the growth of bacteria by damaging DNA and proteins in them with enhanced oxidative stress in bacterial cells [56, 57, 58]. Figure 9(a) depicts the zone of bacterial inhibition imparted by the samples against various bacteria. Figure 9(b) shows the MIC of the samples.

As the $Fe_3O_4$ nanoparticles are ultrafine, they tend to agglomerate readily. It leads to a decrease in their active surface area, which could be a limiting factor for the interaction between bacteria cell walls and these particles. Hence, it lessens the bacterial growth inhibition [59]. As a result, the $Fe_3O_4$ nanoparticles exhibited less antibacterial activity in comparison to G-$Fe_3O_4$ and C-$Fe_3O_4$. The same kind of phenomena might have occurred between the $Fe_3O_4$ nanoparticles distributed over rGO sheets (G-$Fe_3O_4$). However, due to the support of rGO, this material showed enhanced performance compared with bare $Fe_3O_4$ nanoparticles. The efficient surface coating with chitosan might make the $Fe_3O_4$ nanoparticles individual

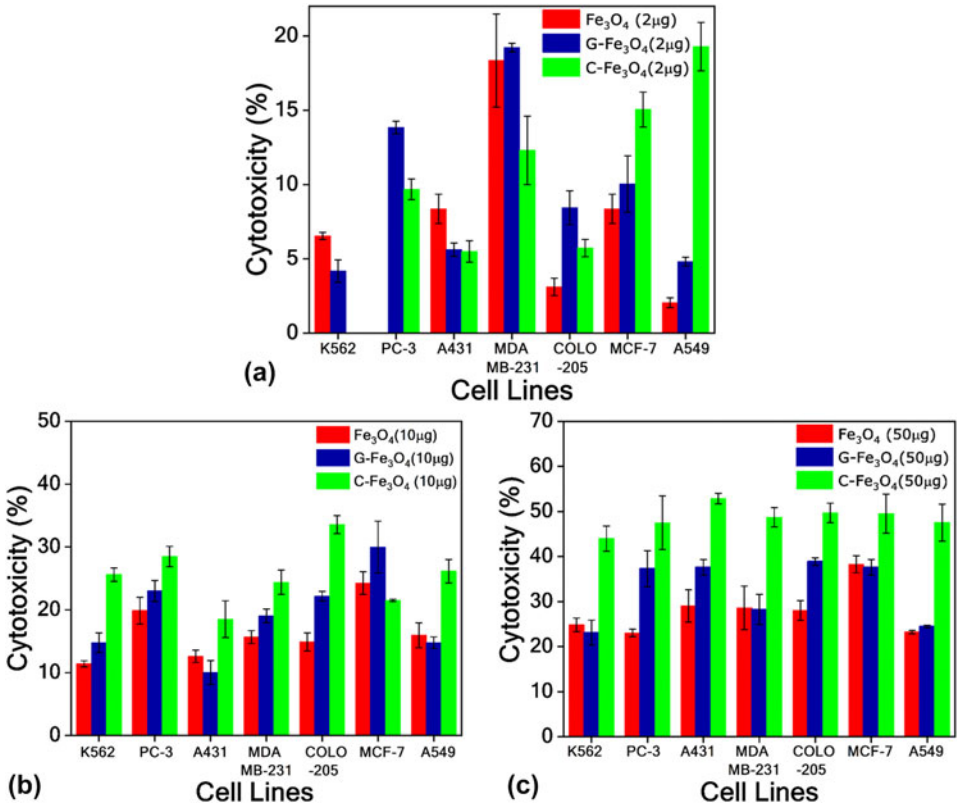



**Figure 8:** Percent cytotoxicity of $Fe_3O_4$, G-$Fe_3O_4$, and C-$Fe_3O_4$ at concentrations of (a) 2 μg/mL, (b) 10 μg/mL, and (c) 50 μg/mL against various cell lines.

https://doi.org/10.1557/jmr.2019.267 Published online by Cambridge University Press



© Materials Research Society 2019

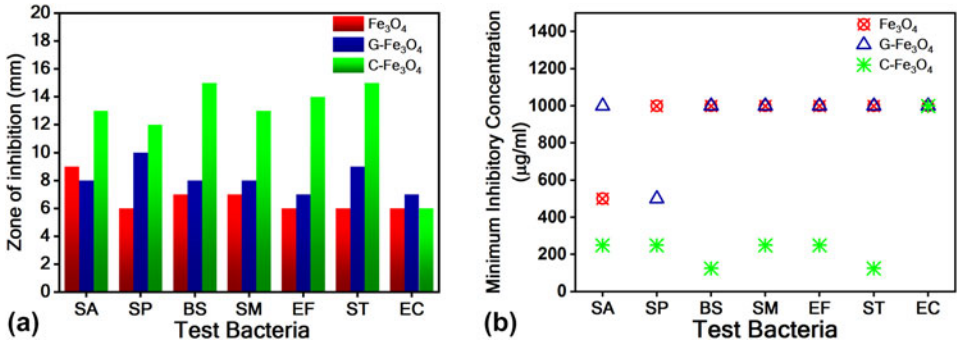



**Figure 9:** (a) Zone of growth inhibition of the samples against various bacteria. SA-*Staphylococcus aureus* (MTCC96), SP-*Streptococcus pyogenes* (MTCC442), BS-*Bacillus subtilis* (MTCC121), SM-*Streptococcus mutans* (MTCC890), EF-*Enterococcus faecalis* (MTCC439), ST-*Salmonella typhi* (MTCC733), and EC-*Escherichia coli* (MTCC723), and (b) MICs of the sample required.

and less agglomerative. Thus, these particles could be penetrated through the bacteria membrane easily and lead to better bactericidal effects [60].

## Conclusions

The present work demonstrates the facile synthesis of $Fe_3O_4$ nanoparticles via chemical coprecipitation method. The inverse spinel structure of magnetite for the particles synthesized was confirmed by XRD analysis. The average particle size was estimated as $6 \pm 3$ nm using TEM. The superparamagnetism of the particles was examined by *M*–*H* hysteresis curves. The rGO was synthesized by electrochemical exfoliation of waste carbon battery electrodes followed by reduction treatment. The $Fe_3O_4$ nanoparticles surfaces were functionalized with chitosan and rGO. Bioactivity tests were performed to quantify cytotoxicity and antibacterial activity of $Fe_3O_4$, G-$Fe_3O_4$, and C-$Fe_3O_4$. The surface functionalization with rGO and chitosan enhanced the cytotoxicity as well as antibacterial activity in comparison to uncoated $Fe_3O_4$ nanoparticles. Majorly, the activity was observed in the descending order as C-$Fe_3O_4$, G-$Fe_3O_4$, and $Fe_3O_4$. Finally, it could be concluded that the agglomeration of the particles might affect their bioactivity negatively.

## Experimental details

### Synthesis of $Fe_3O_4$ nanoparticles and rGO

A simple chemical-coprecipitation technique was adopted for the synthesis of $Fe_3O_4$ nanoparticles. To begin with, anhydrous $FeCl_3$ (96% assay, Fisher Scientific, Mumbai, India) and hydrated $FeCl_2$ (98% assay, Loabachemie, Mumbai, India) were dispersed together in distilled water with the molar ratio of 2:1. The solution was magnetically stirred continuously for 1 h at 70–80 °C under inert ($N_2$) atmosphere. Subsequently, NaOH (96% assay, Fisher Scientific, Mumbai, India) solution of 1 M was added dropwise, which led to the precipitation of solution. The precipitate was separated and washed several times with distilled water and ethanol, and dried in an inert ($N_2$) atmosphere.

The rGO was synthesized via electrochemical exfoliation method followed by thermal reduction treatment. Two waste dry cell battery carbon electrodes were selected as anode and cathode in the process. The complete synthesis details were discussed in our previous work [48].

### Functionalization of $Fe_3O_4$ nanoparticles

The $Fe_3O_4$ nanoparticle surfaces were functionalized with chitosan and rGO individually. For the surface functionalization with chitosan, a surfactant solution was prepared by dissolving 20 mg of chitosan powder in 100 mL of acetic acid solution (1% weight to volume ratio in 100 mL distilled water) and surfactant solution [2 g of CTAB (cetyltrimethylammonium bromide) to 400 mL of distilled water]. Then, $Fe_3O_4$ nanoparticles of 250 mg were dispersed in the surfactant and magnetically stirred for 1 h at 1000 rpm. Afterward, the chitosan-coated $Fe_3O_4$ nanoparticles (C-$Fe_3O_4$) were separated from the solution with the help of the external magnet. The product was cleaned and dried in an oven.

Whereas the rGO functionalized $Fe_3O_4$ nanocomposites (G-$Fe_3O_4$) were obtained by their mechanical mixing (using mortar and pestle) and subsequent heat treatment at 450 °C for 1 h in the nitrogen atmosphere. The as-mentioned heat treatment helps in enhancement of interfacial bonding between the $Fe_3O_4$ nanoparticle and rGO.

### Characterization

XRD spectra of $Fe_3O_4$ nanoparticles were collected using Panalytical X'pert Pro multipurpose diffractometer (MPD; Malvern Panalytical Ltd., Royston, U.K.) in Bragg–Brentano geometry with X'celerator detector with Cu $K_\alpha$ ($\lambda = 1.5406$ Å) radiation (45 kV, 30 mA). The measurements were recorded in the $2\theta$ range of 25–70° with 0.2° step size and 30 s time per

https://doi.org/10.1557/jmr.2019.267 Published online by Cambridge University Press



© Materials Research Society 2019

step. Detailed microstructural and chemical analysis of IONPs were carried out using TITAN $G^2$ 60–300 kV TEM/STEM (FEI, Eindhoven, Netherlands). The high-angle annular dark-field scanning transmission electron microscopy (HAADF-STEM) technique coupled with EDS was used for the elemental mapping/chemical analysis. HRTEM, SAED patterns, and corresponding IFFT images were obtained for phase analysis. The size of each $Fe_3O_4$ particle from dark-field TEM image was measured using ImageJ (v1.52 h) software package after which the particle size distribution histogram was made. The *M–H* hysteresis curve for $Fe_3O_4$ and G-$Fe_3O_4$ was obtained using Lakeshore VSM 7410 in the range of −15 kOe to +15 kOe applied magnetic field. The TGA of $Fe_3O_4$, rGO, and C-$Fe_3O_4$ was carried out using PerkinElmer Diamond TG/DTA (USAA). The thermal stability of samples was examined in the temperature range of 30–800 °C with a heating rate of 10 °C/min in a nitrogen atmosphere. Raman Spectra for rGO, $Fe_3O_4$, and G-$Fe_3O_4$ was recorded using LabRam HP 800 UV Raman spectrometer. The vibrational modes were obtained in the range 800–3200 $cm^{-1}$ using He-Ne laser, 632 nm excitation source.

## Anticancer and antibacterial activity

### *In vitro* cytotoxicity

Cell proliferative studies were conducted on seven different human cancer cell lines taken from various organs, namely, K-562 (erythromyeloblastoid leukemia), PC-3 (h prostate carcinoma), A-431 (epidermoid carcinoma), MDA-MB-231 ($ER^-$ breast carcinoma), COLO-205 (colon carcinoma), MCF-7 ($ER^+$ breast adenocarcinoma), and A-549 (lung carcinoma). The cells were seeded in flat-bottom 96-well plates at desired density ($2 \times 10^3$) in 100 µL of the medium. The materials were sterilized by dissolving in DMSO, and the solutions were filtered through a 0.22-µm filter. Cells were treated with 2 µg/mL, 10 µg/mL, and 50 µg/mL of test material ($Fe_3O_4$, C-$Fe_3O_4$, and G-$Fe_3O_4$) and incubated for 24 h. 20 µL of MTT solution (5 mg/mL) was added to each well (i.e., 50 µg/well) and incubated at 37 °C for 4 h before the termination of the assay. The culture medium of plates was decanted on blotting paper, and 150 µL of DMSO was added to each well. The plates were agitated on a plate shaker for 5 min, and optical density was measured at 570 nm with the help of spectrophotometer (Thermo Fisher Scientific, Waltham, Massachusetts). Cell viability was calculated by comparing absorbance of treated versus untreated cells. Growth inhibition was calculated by subtracting cell growth from 100.

### Antibacterial activity

The antibacterial activity was tested against a panel of pathogenic bacteria, which were purchased from Microbial Type Culture Collection (MTCC) of CSIR-IMTECH, Chandigarh, India. Lyophilized bacterial strains were cultured overnight at 37 °C in nutrient broth (Himedia Ltd., Mumbai, India). Each of the bacterial strain was revived in liquid media for experimentation. The turbidity of the log phase was adjusted to 0.5 McFarland equivalents (approximately 1–2 × $10^8$ cfu/mL). Antibacterial activity of $Fe_3O_4$, C-$Fe_3O_4$, and G-$Fe_3O_4$ was examined against various Gram-positive bacteria viz., *Staphylococcus aureus* (SA, MTCC96), *Streptococcus pyogenes* (SP, MTCC442), *Bacillus subtilis* (BS, MTCC121), *Streptococcus mutans* (SM, MTCC890), and *Enterococcus faecalis* (EF, MTCC439), as well as Gram-negative bacteria, namely, *Salmonella typhi* (ST, MTCC733) and *Escherichia coli* (EC, MTCC723). The antibacterial activity of synthesized nanoparticles was determined in terms of minimum inhibitory concentration (MIC; a quantitative analysis) and zone of inhibition (ZOI; a qualitative analysis). For determining MIC, two-fold serial dilution technique was used against the bacterial strains [61]. For the experiments, 10 wells of 96-well plates in series were filled with a broth containing nanoparticles in such a way that the concentration of the solution in the subsequent tube reducing to one-half, 11th, and 12th well were used as untreated and media vehicle control, respectively. The tests were performed individually on three test compounds, namely, $Fe_3O_4$, C-$Fe_3O_4$, and G-$Fe_3O_4$. The test compounds were added to the first well of each row simultaneously (in three separate test tubes) and mixed thoroughly. From the above three test tubes, half of the media containing test molecules were transferred to the 2nd set of test tubes and mixed gently. The same procedure was repeated till the 10th well. Properly diluted log phase culture of bacteria (10 µL, test organism) with a titer of $10^4$ cfu/mL was added to each of the wells mentioned above. The procedure was followed with tubes incubation at 37 °C, and then turbidity was measured.

ZOI was determined by a disc diffusion assay method [62]. The process starts with the preparation of bacterial inoculums from 24 h overnight cultures in nutrient broth solution with the turbidity of 1.5 × $10^8$ cfu/mL. 100 µL aliquots of inoculums (divided samples of IONPs) were put on agar plate surface by using sterile glass spreader. A paper disc (Whatman filter paper 3) of 5 mm diameter taken with 5 µL of test molecule from 100 mg/mL stock was kept. The disc was then air-dried and placed on the nutrient agar plates. The plates were incubated at 37 °C for 16–24 h. The ZOI of complete bacterial growth was then calculated in mm.

## Acknowledgments

The authors are grateful to Mr. S.L. Gadge for his constant support and motivation for the work. Mr. Devthade Vidyasagars's extended support is uncountable. The SAIF-IIT Bombay support for TGA experiments is greatly acknowledged.

https://doi.org/10.1557/jmr.2019.267 Published online by Cambridge University Press



© Materials Research Society 2019

## References


1. **M. Nazarenus, Q. Zhang, M.G. Soliman, P. del Pino, B. Pelaz, S. Carregal-Romero, J. Rejman, B. Rothen-Rutishauser, M.J.D. Clift, R. Zellner, G.U. Nienhaus, J.B. Delehanty, I.L. Medintz, and W.J. Parak**: In vitro interaction of colloidal nanoparticles with mammalian cells: What have we learned thus far? *Beilstein J. Nanotechnol.* **5**, 1477 (2014).
2. **G. Baldi, D. Bonacchi, C. Innocenti, G. Lorenzi, and C. Sangregorio**: Cobalt ferrite nanoparticles: The control of the particle size and surface state and their effects on magnetic properties. *J. Magn. Magn. Mater.* **311**, 10 (2007).
3. **Q. Song and Z.J. Zhang**: Shape control and associated magnetic properties of spinel cobalt ferrite nanocrystals. *J. Am. Chem. Soc.* **126**, 6164 (2004).
4. **P. Kucheryavy, J. He, V.T. John, P. Maharjan, L. Spinu, G.Z. Goloverda, and V.L. Kolesnichenko**: Superparamagnetic iron oxide nanoparticles with variable size and an iron oxidation state as prospective imaging agents. *Langmuir* **29**, 710 (2013).
5. **N.A. Frey, S. Peng, K. Cheng, and S. Sun**: Magnetic nanoparticles: Synthesis, functionalization, and applications in bioimaging and magnetic energy storage. *Chem. Soc. Rev.* **27**, 2532 (2009).
6. **V. Polshettiwar, R. Luque, A. Fihri, H. Zhu, M. Bouhrara, and J.M. Basset**: Magnetically recoverable nanocatalysts. *Chem. Rev.* **111**, 3036 (2011).
7. **P.A. Mangrulkar, V. Polshettiwar, N.K. Labhsetwar, R.S. Varma, and S.S. Rayalu**: Nano-ferrites for water splitting: Unprecedented high photocatalytic hydrogen production under visible light. *Nanoscale* **4**, 5202 (2012).
8. **R.H. Goncalves and E.R. Leite**: Nanostructural characterization of mesoporous hematite thin film photoanode used for water splitting. *J. Mater. Res.* **29**, 47 (2014).
9. **C.S.S.R. Kumar and F. Mohammad**: Magnetic nanomaterials for hyperthermia-based therapy and controlled drug delivery. *Adv. Drug Delivery Rev.* **63**, 789 (2011).
10. **A.B. Salunkhe, V.M. Khot, and S.H. Pawar**: Magnetic hyperthermia with magnetic nanoparticles: A status review. *Curr. Top. Med. Chem.* **14**, 572 (2014).
11. **R. Qiao, C. Yang, and M. Gao**: Superparamagnetic iron oxide nanoparticles: From preparations to in vivo MRI applications. *J. Mater. Chem.* **19**, 6274 (2009).
12. **T. Macher, J. Totenhagen, J. Sherwood, Y. Qin, D. Gurler, M.S. Bolding, and Y. Bao**: Ultrathin iron oxide nanowhiskers as positive contrast agents for magnetic resonance imaging. *Adv. Funct. Mater.* **25**, 490 (2015).
13. **M. Iv, N. Telischak, D. Feng, S. Holdsworth, K. Yeom, and H. Daldrup-Link**: Clinical applications of iron oxide nanoparticles for magnetic resonance imaging of brain tumors. *Nanomedicine* **10**, 993 (2015).
14. **P.W. Goodwill and S.M. Conolly**: Experimental demonstration of *X*-space magnetic particle imaging. *SPIE Proc. Med. Imaging* **7965**, 79650U (2011).
15. **R.M. Ferguson, A.P. Khandhar, and K.M. Krishnan**: Tracer design for magnetic particle imaging (invited). *J. Appl. Phys.* **111**, 07B318 (2012).
16. **A. Tomitaka, H. Arami, S. Gandhi, and K.M. Krishnan**: Lactoferrin conjugated iron oxide nanoparticles for targeting brain glioma cells in magnetic particle imaging. *Nanoscale* **7**, 16890 (2015).
17. **M.P. Marszałł**: Application of magnetic nanoparticles in pharmaceutical sciences. *Pharm. Res.* **28**, 480 (2011).
18. **G. Zhang, F. Qie, J. Hou, S. Luo, L. Luo, X. Sun, and T. Tan**: One-pot solvothermal method to prepare functionalized $Fe_3O_4$ nanoparticles for bioseparation. *J. Mater. Res.* **27**, 1006 (2012).
19. **K.J. Widder, A.E. Senyei, and D.G. Scarpelli**: Magnetic microspheres: A model system for site specific drug delivery in vivo. *Exp. Biol. Med.* **158**, 141 (1978).
20. **S. Laurent, S. Dutz, U.O. Häfeli, and M. Mahmoudi**: Magnetic fluid hyperthermia: Focus on superparamagnetic iron oxide nanoparticles. *Adv. Colloid Interface Sci.* **166**, 8 (2011).
21. **F. Assa, H. Jafarizadeh-Malmiri, H. Ajamein, H. Vaghari, N. Anarjan, O. Ahmadi, and A. Berenjian**: Chitosan magnetic nanoparticles for drug delivery systems. *Crit. Rev. Biotechnol.* **37**, 492 (2017).
22. **H. Salehizadeh, E. Hekmatian, M. Sadeghi, and K. Kennedy**: Synthesis and characterization of core–shell $Fe_3O_4$–gold–chitosan nanostructure. *J. Nanobiotechnol.* **10**, 3 (2012).
23. **P.R. Roper and B. Drewinko**: Comparison of in vitro methods to determine drug-induced cell lethality. *Cancer Res.* **36**, 2182 (1976).
24. **C. Valgas, S. Machado de Souza, E.F. A Smânia, and A. Smânia, Jr**: Screening methods to determine antibacterial activity of natural products. *Braz. J. Microbiol.* **38**, 369 (2007).
25. **F. Perreault, A.F. De Faria, S. Nejati, and M. Elimelech**: Antimicrobial properties of graphene oxide nanosheets: Why size matters. *ACS Nano* **9**, 7226 (2015).
26. **S. Gurunathan, J. Woong Han, V. Eppakayala, and J. Kim**: Green synthesis of graphene and its cytotoxic effects in human breast cancer cells. *Int. J. Nanomed.* **8**, 1015 (2013).
27. **C.M. Santos, J. Mangadlao, F. Ahmed, A. Leon, R.C. Advincula, and D.F. Rodrigues**: Graphene nanocomposite for biomedical applications: Fabrication, antimicrobial and cytotoxic investigations. *Nanotechnology* **23**, 395101 (2012).
28. **M. Pelin, L. Fusco, V. León, C. Martín, A. Criado, S. Sosa, E. Vázquez, A. Tubaro, and M. Prato**: Differential cytotoxic effects of graphene and graphene oxide on skin keratinocytes. *Sci. Rep.* **7**, 1 (2017).
29. **V. Hastak, S. Bandi, S. Kashyap, S. Singh, S. Luqman, M. Lodhe, D.R. Peshwe, and A.K. Srivastav**: Antioxidant efficacy of chitosan/graphene functionalized superparamagnetic iron oxide nanoparticles. *J. Mater. Sci.: Mater. Med.* **29**, 154 (2018).


https://doi.org/10.1557/jmr.2019.267 Published online by Cambridge University Press



© Materials Research Society 2019

30. **Z. Yang, X. Hao, S. Chen, Z. Ma, W. Wang, C. Wang, L. Yue, H. Sun, Q. Shao, V. Murugadoss, and Z. Guo**: Long-term antibacterial stable reduced graphene oxide nanocomposites loaded with cuprous oxide nanoparticles. *J. Colloid Interface Sci.* **533**, 13 (2019).
31. **M. Jedrzejczak-Silicka**: Cytotoxicity and genotoxicity of GO–$Fe_3O_4$ hybrid in cultured mammalian cells. *Pol. J. Chem. Technol.* **19**, 27 (2017).
32. **N.E. Gade, R.M. Dar, O.P. Mishra, J.R. Khan, V. Kumar, and A. Patyal**: Evaluation of dose-dependent cytotoxic effects of graphene oxide-iron oxide nanocomposite on caprine Wharton's jelly derived mesenchymal stem cells. *J. Anim. Res.* **5**, 415 (2015).
33. **G.D. Gatta, I. Kantor, T.B. Ballaran, L. Dubrovinsky, and C. Mccammon**: Effect of non-hydrostatic conditions on the elastic behaviour of magnetite: An in situ single-crystal X-ray diffraction study. *Phys. Chem. Miner.* **34**, 627 (2007).
34. **E. Prince, E. Prince, and J.K. Stalick**: *Accuracy in Powder Diffraction II*, Vol. **846** (NIST Special Publicaiton, Gaithersburg, MD, 1992).
35. **A.K. Srivastav, A.M. Panindre, and B.S. Murty**: XRD characterization of microstructural evolution during mechanical alloying of W–20 wt% Mo. *Trans. Indian Inst. Met.* **66**, 409 (2013).
36. **S. Bandi, V. Hastak, D.R. Peshwe, and A.K. Srivastav**: In situ $TiO_2$–rGO nanocomposites for CO gas sensing. *Bull. Mater. Sci.* **41**, 115 (2018).
37. **D. Balzar and H. Ledbetter**: Voigt-function modeling in Fourier analysis of size-and strain-broadened X-ray diffraction peaks. *J. Appl. Crystallogr.* **26**, 97 (1993).
38. **D. Balzar**: NIST (2012). Available at: http://www.boulder.nist.gov/div853/balzar/breadth.htm.
39. **A.K. Srivastav, J. Basu, S. Kashyap, N. Chawake, D. Yadav, and B.S. Murty**: Crystallographic-shear-phase-driven $W_{18}O_{49}$ nanowires growth on nanocrystalline W surfaces. *Scr. Mater.* **115**, 28 (2016).
40. **B.D. Cullity and C.D. Graham**: *Introduction to Magnetic Materials* (John Wiley & Sons, Inc., Hoboken, New Jersey, 2008). ISBN: 978-0-471-47741-9 47741.
41. **D. Padalia, U.C. Johri, and M.G.H. Zaidi**: Study of cerium doped magnetite ($Fe_3O_4$:Ce)/PMMA nanocomposites. *Phys. B* **407**, 838 (2012).
42. **X.N. Pham, T.P. Nguyen, T.N. Pham, T.T.N. Tran, and T.V.T. Tran**: Synthesis and characterization of chitosan-coated magnetite nanoparticles and their application in curcumin drug delivery. *Adv. Nat. Sci. Nanosci. Nanotechnol.* **7**, 045010 (2016).
43. **J. Safari and L. Javadian**: Chitosan decorated $Fe_3O_4$ nanoparticles as a magnetic catalyst in the synthesis of phenytoin derivatives. *RSC Adv.* **4**, 48973 (2014).
44. **I. Karimzadeh, M. Aghazadeh, T. Doroudi, M.R. Ganjali, and P.H. Kolivand**: Electrochemical preparation and characterization of chitosan-coated superparamagnetic iron oxide ($Fe_3O_4$) nanoparticles. *Mater. Res. Innovations* **1** (2017).
45. **J. Bin Wu, M.L. Lin, X. Cong, H.N. Liu, and P.H. Tan**: Raman spectroscopy of graphene-based materials and its applications in related devices. *Chem. Soc. Rev.* **47**, 1822 (2018).
46. **S. Mura, Y. Jiang, I. Vassalini, A. Gianoncelli, I. Alessandri, G. Granozzi, L. Calvillo, N. Senes, S. Enzo, P. Innocenzi, and L. Malfatti**: Graphene oxide/iron oxide nanocomposites for water remediation. *ACS Appl. Nano Mater.* **1**, 6724 (2018).
47. **M. Wall**: The Raman spectroscopy of graphene and the determination of layer thickness. *Thermo Sci. Appl.*, 52252 (2011). Available at: http://tools.thermofisher.com/content/sfs/brochures/AN52252_E%201111%20LayerThkns_H_1.pdf.
48. **S. Bandi, S. Ravuri, D.R. Peshwe, and A.K. Srivastav**: Graphene from discharged dry cell battery electrodes. *J. Hazard. Mater.* **366**, 358 (2019).
49. **H. Wang, Y. Wang, X. Cao, M. Feng, and G. Lan**: Vibrational properties of graphene and graphene layers. *J. Raman Spectrosc.* **40**, 1791 (2009).
50. **I. Corazzari, R. Nisticò, F. Turci, M.G. Faga, F. Franzoso, S. Tabasso, and G. Magnacca**: Advanced physico-chemical characterization of chitosan by means of TGA coupled on-line with FTIR and GCMS: Thermal degradation and water adsorption capacity. *Polym. Degrad. Stab.* **112**, 1 (2015).
51. **A. Hasan, G. Waibhaw, S. Tiwari, K. Dharmalingam, I. Shukla, and L.M. Pandey**: Fabrication and characterization of chitosan, polyvinylpyrrolidone, and cellulose nanowhiskers nanocomposite films for wound healing drug delivery application. *J. Biomed. Mater. Res., Part A* **105**, 2391 (2017).
52. **A. Tayyebi and M. Outokesh**: Supercritical synthesis of a magnetite-reduced graphene oxide hybrid with enhanced adsorption properties toward cobalt & strontium ions. *RSC Adv.* **6**, 13898 (2016).
53. **S.F. Shi, J.F. Jia, X.K. Guo, Y.P. Zhao, D.S. Chen, Y.Y. Guo, T. Cheng, and X.L. Zhang**: Biocompatibility of chitosan-coated iron oxide nanoparticles with osteoblast cells. *Int. J. Nanomedicine* **7**, 5593 (2012).
54. **T. Kavinkumar, K. Varunkumar, V. Ravikumar, and S. Manivannan**: Anticancer activity of graphene oxide-reduced graphene oxide–silver nanoparticle composites. *J. Colloid Interface Sci.* **505**, 1125 (2017).
55. **J.M. Andrews**: Determination of minimum inhibitory concentrations. *J. Antimicrob. Chemother.* **48**, 5 (2001).
56. **B. Uygur, G. Craig, M.D. Mason, and A.K. Ng**: Cytotoxicity and Genotoxicity of Silver Nanoparticles in Human Cells. *Tech. Proc. 2009 NSTI Nanotechnol. Conf. Expo, NSTI-Nanotech 2009* **2**, 383 (2009).
57. **S.M. Hussain, K.L. Hess, J.M. Gearhart, K.T. Geiss, and J.J. Schlager**: In vitro toxicity of nanoparticles in BRL 3A rat liver cells. *Toxicol. In Vitro* **19**, 975 (2005).
58. **D.K. Padhi, T.K. Panigrahi, K. Parida, S.K. Singh, and P.M. Mishra**: Green synthesis of $Fe_3O_4$/RGO nanocomposite with enhanced photocatalytic performance for Cr(VI) reduction, phenol

https://doi.org/10.1557/jmr.2019.267 Published online by Cambridge University Press



© Materials Research Society 2019

degradation, and antibacterial activity. *ACS Sustainable Chem. Eng.* **5**, 10551 (2017).

59. **A. Nayamadi Mahmoodabadi, A. Kompany, and M. Mashreghi**: Characterization, antibacterial and cytotoxicity studies of graphene–$Fe_3O_4$ nanocomposites and $Fe_3O_4$ nanoparticles synthesized by a facile solvothermal method. *Mater. Chem. Phys.* **213**, 285 (2018).
60. **C. Lee, J.Y. Kim, W. Il Lee, K.L. Nelson, J. Yoon, and D.L. Sedlak**: Bactericidal effect of zero-Valent iron nanoparticles on *Escherichia coli*. *Environ. Sci. Technol.* **42**, 4927 (2008).
61. **V. Srivastava, M.P. Darokar, A. Fatima, J.K. Kumar, C. Chowdhury, H.O. Saxena, G.R. Dwivedi, K. Shrivastava, V. Gupta, S.K. Chattopadhyay, S. Luqman, M.M. Gupta, A.S. Negi, and S.P.S. Khanuja**: Synthesis of diverse analogues of Oenostacin and their antibacterial activities. *Bioorg. Med. Chem.* **15**, 518 (2007).
62. **S. Luqman, G.R. Dwivedi, M.P. Darokar, A. Kalra, and S.P.S. Khanuja**: Antimicrobial activity of Eucalyptus citriodora essential oil. *Int. J. Essent. Oil Ther.* **2**, 69 (2008).

https://doi.org/10.1557/jmr.2019.267 Published online by Cambridge University Press



© Materials Research Society 2019